An approach for predicting stress-induced anisotropy around a borehole

Citation: Fang, Xinding, Michael Fehler, Zhenya Zhu, Tianrun Chen, Stephen Brown, Arthur Cheng, and M. Nafi Toksoz. "An approach for predicting stress-induced anisotropy around a borehole." GEOPHYSICS 78, no. 3 (April 11, 2013): D143-D150. © 2013 Society of Exploration Geophysicists

As Published: http://dx.doi.org/10.1190/geo2012-0145.1

Publisher: Society of Exploration Geophysicists

Persistent URL: http://hdl.handle.net/1721.1/81404

Version: Final published version: final published article, as it appeared in a journal, conference proceedings, or other formally published context

GEOPHYSICS, VOL. 78, NO. 3 (MAY-JUNE 2013); P. D143–D150, 13 FIGS., 2 TABLES.
10.1190/GEO2012-0145.1

An approach for predicting stress-induced anisotropy around a borehole

Xinding Fang[1], Michael Fehler[1], Zhenya Zhu[1], Tianrun Chen[2], Stephen Brown[1], Arthur Cheng[2], and M. Nafi Toksöz[1]

ABSTRACT

Formation elastic properties near a borehole may be altered from their original state due to the stress concentration around the borehole. This could result in a biased estimation of formation properties but could provide a means to estimate in situ stress from sonic logging data. To properly account for the formation property alteration, we propose an iterative numerical approach to calculate stress-induced anisotropy around a borehole by combining a rock physics model and a finite-element method. We tested the validity and accuracy of our approach by comparing numerical results to laboratory measurements of the stress-strain relation of a sample of Berea sandstone, which contains a borehole and is subjected to a uniaxial stress loading. Our iterative approach converges very fast and can be applied to calculate the spatially varying stiffness tensor of the formation around a borehole for any given stress state.

INTRODUCTION

Borehole logging data provide an important way to interpret rock anisotropy and estimate the in situ stress state (Mao, 1987; Sinha and Kostek, 1995). Typically, the anisotropy in intact rocks includes intrinsic and stress-induced components (Jaeger et al., 2007). Intrinsic anisotropy can be caused by bedding, microstructure, or aligned fractures, whereas stress-induced anisotropy is caused by the opening or closing of the compliant and cracklike parts of the pore space due to tectonic stresses. Most unfractured reservoir rocks, such as sands, sandstones and carbonates, have very little intrinsic anisotropy in an unstressed state (Wang, 2002). Drilling a borehole in a formation significantly alters the local stress distribution. When the in situ stresses are anisotropic, drilling causes the closure or opening of cracks in rocks around the borehole and leads to an additional stress-induced anisotropy. To properly include this additional stress-induced anisotropy during inversion for formation properties and the in situ stress estimation from logging data, a thorough analysis needs to consider the constitutive relation between the complex stress field applied around a borehole and the stiffness tensor of a rock with microcracks embedded in the matrix (Brown and Cheng, 2007).

Three theoretical approaches have been proposed to calculate stress-related anisotropy around a borehole. The first approach (Sinha and Kostek, 1996; Winkler et al., 1998) used the acoustoelastic model, which gives a nonlinear stress-strain relationship (Johnson and Rasolofosaon, 1996), to calculate the stress-induced azimuthal velocity changes around a borehole. The velocity variation with applied stresses is accounted for through the use of the third-order elastic constants, which are obtained through compression experiments on rock samples. The second approach (Tang et al., 1999; Tang and Cheng, 2004) used an empirical stress-velocity coupling relation to estimate the variation of shear elastic constants (C_{44} and C_{55}) as a function of stress. In this approach, the square of the shear wave velocities propagating along a borehole with different polarizations are assumed to be linearly proportional to the stresses applied normal to the borehole axis. This approach is used for studying shear wave splitting in a borehole and only gives the values of shear elastic constants (i.e., C_{44} and C_{55}) instead of the full elastic stiffness tensor. However, these two approaches have no rock physics basis because they ignore the constitutive relationship between an anisotropic applied stress field and the stiffness tensor for a rock (Brown and Cheng, 2007). They thus give approximate solutions. Also, they are based on an assumption of plane strain, which considers formation properties to be invariant along the borehole axis and the applied stresses are normal to the borehole axis. Brown and Cheng (2007) propose the third approach to calculate stress-induced

Manuscript received by the Editor 30 April 2012; revised manuscript received 1 November 2012; published online 11 April 2013.
[1]Massachusetts Institute of Technology, Department of Earth, Atmospheric and Planetary Sciences, Cambridge, Massachusetts, USA. E-mail: xinfang@mit.edu; fehler@mit.edu; zhenya@mit.edu; srbrown@mit.edu; toksoz@mit.edu.
[2]Halliburton, Houston, Texas, USA. E-mail: tianrunchen@hotmail.com; arthur.cheng@halliburton.com.

anisotropy around a borehole embedded in an *anisotropic* medium. In their model, the stress-dependent stiffness tensor of anisotropic rocks is calculated using a general fabric tensor model (Oda, 1986; Oda et al., 1986). The intrinsic relation between stress and stiffness of a rock is accounted for through the use of a rock physics model, which is not included in the methods of Sinha and Kostek (1996) and Tang et al. (1999). The approach of Brown and Cheng (2007) reflects the physics of stress-induced anisotropy and thus is more accurate. However, the general fabric tensor model requires the prior knowledge of crack geometries (i.e., crack shapes and aspect ratio spectra) and distributions, which may not always be available in field applications. In this paper, we replace the general fabric tensor model with the model of Mavko et al. (1995), which assumes the crack orientation distribution in the rock matrix in an unstressed state to be uniform and isotropic. Under this assumption, rocks are still isotropic when subjected to a hydrostatic stress and become anisotropic under an anisotropic stress loading. Anisotropy is induced through closing of the compliant part of the pore space, which includes microcracks and grain boundaries (Sayers, 1999, 2002). Detailed information about pores/cracks is not required in Mavko's model, and the effect of pore/crack *closure* is implicitly determined by the relation between elastic wave velocities of the rock and the applied hydrostatic pressure obtained from laboratory data. Another major assumption of Mavko's model is that the anisotropy induced by pore/crack *opening* is negligible.

BRIEF REVIEW OF MAVKO'S METHOD

Mavko et al. (1995) propose a simple and practical method to estimate the generalized pore space compliance of rocks using experimental data of rock velocity versus hydrostatic pressure. The approach Mavko et al. (1995) propose for calculating the stiffness tensor with stress-induced anisotropy at a stress state σ uses the following steps:

1) Calculate the pressure-dependent isotropic elastic compliances $S^{\text{iso}}_{ijkl}(p)$ from measurements of compression (P) and shear wave (S) velocities versus hydrostatic pressure. The compliance S^{0}_{ijkl} at the largest measured pressure, under which most of the compliant parts of the pore space are closed, is chosen as a reference point. The additional compliance $\Delta S^{\text{iso}}_{ijkl}(p)$ due to the presence of pore space at pressure p is defined to be $S^{\text{iso}}_{ijkl}(p) - S^{0}_{ijkl}$. Note that at a pressure p less than the largest measured pressure, there is more pore volume than at the highest pressure and the compliance is larger.
2) Calculate the pressure-dependent crack normal compliance $W_N(p)$ and crack tangential compliance $W_T(p)$ from $\Delta S^{\text{iso}}_{ijkl}(p)$ via

$$W_N(p) = \frac{1}{2\pi}\Delta S^{\text{iso}}_{jjkk}(p) \tag{1}$$

and

$$W_T(p) = W_N(p)\frac{\Delta S^{\text{iso}}_{jkjk}(p) - \Delta S^{\text{iso}}_{jjkk}(p)}{4\Delta S^{\text{iso}}_{jjkk}(p)}, \tag{2}$$

where the repeated indices in $\Delta S^{\text{iso}}_{jjkk}(p)$ and $\Delta S^{\text{iso}}_{jkjk}(p)$ mean summation. The factor $\frac{1}{2\pi}$ comes from the average of crack compliance over all solid angles.
3) Calculate the stress-induced compliance $\Delta S_{ijkl}(\sigma)$ through

$$\begin{aligned}\Delta S_{ijkl}(\sigma) = &\int_{\theta=0}^{\pi/2}\int_{\phi=0}^{2\pi} W_N(m^T\sigma m) m_i m_j m_k m_l \sin\theta \mathrm{d}\theta\mathrm{d}\phi \\ &\int_{\theta=0}^{\pi/2}\int_{\phi=0}^{2\pi} W_T(m^T\sigma m)[\delta_{ik}m_j m_l + \delta_{il}m_j m_k \\ &+\delta_{jk}m_i m_l + \delta_{jl}m_i m_k - 4m_i m_j m_k m_l]\sin\theta \mathrm{d}\theta\mathrm{d}\phi, \end{aligned} \tag{3}$$

where σ is a 3×3 stress tensor, $m = (\sin\theta\cos\phi, \sin\theta\sin\phi, \cos\theta)^T$ is the unit normal to the crack surface, and θ and ϕ are the polar and azimuthal angles in a spherical coordinate system. Note that $W_N(p)$ and $W_T(p)$ in equations 1 and 2 have been replaced by $W_N(m^T\sigma m)$ and $W_T(m^T\sigma m)$ in equation 3, assuming that the crack closure is determined by the normal stress, $m^T\sigma m$, acting on the crack surface. The stress tensor σ needs to be projected onto the normal directions of the crack surfaces.
4) Obtain the stiffness tensor $C_{ijkl}(\sigma)$ by inverting $S^{0}_{ijkl} + \Delta S_{ijkl}(\sigma)$.

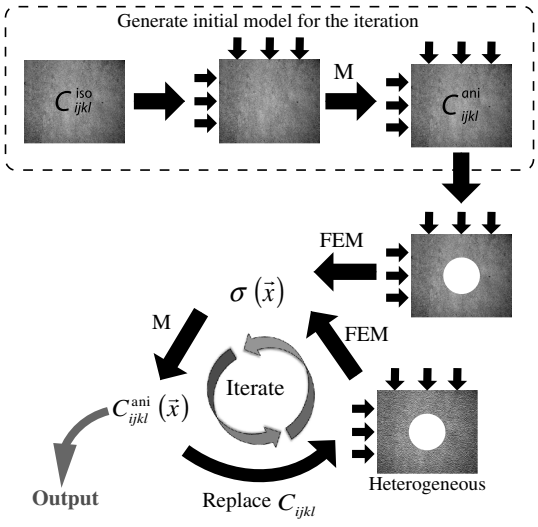

Figure 1. Workflow for computation of stress-induced anisotropy around a borehole. "FEM" and "M" represent the finite-element method and the method of Mavko et al. (1995), respectively.

WORKFLOW FOR THE NUMERICAL MODELING

The method of Mavko et al. (1995) can be applied to calculate the stress-induced anisotropy in homogeneous rocks, as discussed in the Introduction. When a borehole is drilled in a rock subjected to an anisotropic stress loading, the local stress field around the borehole is changed and causes rock anisotropy. Similar to the procedure Brown and Cheng (2007) propose, in this paper, we investigate this stress-induced anisotropy around a borehole at a given stress state by combining the method of Mavko et al. (1995) and a numerical approach illustrated in Figure 1.

We first begin with a homogeneous isotropic intact rock model C^{iso}_{ijkl}, on which Mavko's model is based. The intact rock refers to the rock before the borehole is drilled. After experimentally obtaining the P- and S-wave velocity data as a function of hydrostatic pressure, we apply equation 3 to calculate the anisotropic stiffness tensor C^{ani}_{ijkl} of the intact rock under stress σ, which can be

anisotropic. Next, we drill a borehole in the model and use the calculated C_{ijkl}^{ani} as the input in our initial model containing a borehole. The current C_{ijkl}^{ani} does not include the effect from stress change due to the borehole. We apply a finite-element method (FEM) to calculate the spatially varying stress field within the model including the borehole for a given stress loading σ and the initial anisotropic C_{ijkl}^{ani}. From the output of the FEM, we can obtain the local stress tensor $\sigma(\mathbf{x})$ and then calculate a new stiffness tensor $C_{ijkl}^{\text{ani}}(\mathbf{x})$ as a function of space applying equation 3. The new $C_{ijkl}^{\text{ani}}(\mathbf{x})$ becomes heterogeneous and includes the effect of the borehole. We keep iterating the above steps by calling the FEM and applying equation 3 until $C_{ijkl}^{\text{ani}}(\mathbf{x})$ converges. We use the following as a convergence criterion:

$$\text{Convergence}(m) = \frac{1}{N}\sum_{n=1}^{N}\sqrt{\frac{\sum_{ijkl}[C_{ijkl}^{m}(x_n) - C_{ijkl}^{m-1}(x_n)]^2}{\sum_{ijkl}[C_{ijkl}^{m-1}(x_n)]^2}}, \tag{4}$$

where m indicates the mth iteration, N is the total number of spatial sampling points of the model, $\sum_{ijkl}$ means the summation over 21 independent elastic constants. Convergence(m) indicates the percentage change of the model stiffness after the mth iteration comparing to the model at the $(m-1)$th iteration. We define C_{ijkl} to have converged when Convergence(m) <1%. Convergence means that C_{ijkl} and the stress field are consistent and Hooke's law is satisfied: the model is under static equilibrium. Finally, we can obtain the spatial distribution of the anisotropic elastic constants $C_{ijkl}(\mathbf{x})$ around a borehole for the given stress state as the output of our numerical simulation. In our approach, density is assumed to be independent of the applied stress because the change of density caused by stress loading is negligible (Coyner, 1984).

In our approach, we assume that stress-induced anisotropy is caused by the closure of cracks/pores due to the applied compressive stress on their surfaces and the effect of tensile stress is negligible. This assumption brings up two issues: (1) How important is the tensile stress in the earth? (2) How do we deal with the tensile stress in our calculation? We will discuss these below.

For a homogeneous isotropic elastic rock, the circumferential stress σ_θ and the radial stress σ_r around a circular borehole subjected to minimum and maximum principal stresses (S_h and S_H) are given by (for example, Tang and Cheng, 2004)

$$\sigma_\theta = \frac{1}{2}(S_H + S_h)\left(1 + \frac{R^2}{r^2}\right) - \frac{1}{2}(S_H - S_h)\left(1 + 3\frac{R^4}{r^4}\right)\cos 2\theta, \tag{5}$$

$$\sigma_r = \frac{1}{2}(S_H + S_h)\left(1 - \frac{R^2}{r^2}\right) + \frac{1}{2}(S_H - S_h)\left(1 - 4\frac{R^2}{r^2} + 3\frac{R^4}{r^4}\right)\cos 2\theta, \tag{6}$$

where R is the borehole radius, r is the distance from the center of the borehole, and θ is the azimuth measured from the direction of S_H.

The compressive stress $\sigma_\theta + \sigma_r$ around the borehole provides an indication of how velocity around the borehole is affected by stress concentration. The $\sigma_\theta + \sigma_r$ has maximum and minimum values at the wellbore, and $\sigma_r = 0$ at $r = R$, so the stress field at the wellbore is dominated by σ_θ, which has the maximum value $\sigma_\theta = 3S_H - S_h$ at $\theta = \pm 90^\circ$ and the minimum value $\sigma_\theta = 3S_h - S_H$ at $\theta = 0^\circ$ and 180°. In situ, S_H and S_h are present, and $S_H \le 3S_h$ in most cases (Brace and Kohlstedt, 1980; Zoback et al., 1985), thus the minimum $\sigma_\theta = 3S_h - S_H \ge 0$ is compressive. In this sense, there is no tensile stress around the borehole.

However, the condition $S_H \le 3S_h$ may not be satisfied in laboratory experiments. Uniaxial compression experiments (i.e., $S_h = 0$), which would induce significant tensile stress around the borehole, have been conducted for the study of stress-induced velocity change around a borehole by many researchers (Winkler, 1996; Winkler et al., 1998; Tang and Cheng, 2004). The change of rock elastic properties caused by tensile stress is usually unknown. Traditional methods (Sinha and Kostek, 1996; Tang et al., 1999) for calculating the stress-dependent velocity around a borehole use the data measured from compression experiments to estimate either the third-order elastic constants or empirical coefficients, which relate the rock velocity change to the applied stresses. For the case of uniaxial stress, Sinha and Kostek (1996) and Tang et al. (1999) base their equations on compression experiment data to predict the velocity in the tensile stress regions. This kind of extrapolation has no physical basis and could result in underestimation of the velocity in the regions around $\theta = 0^\circ$ and 180°. A schematic explanation is shown in Figure 2a. The solid curve represents the data measured in a compression experiment, and the dashed curve indicates the extrapolation of the data to the tensile stress (stress < 0) region, which may incorrectly predict low velocity in this region. Different kinds of rock would respond to tensile stress differently due to varying microcrack structure and rock strength. For Berea sandstone, which is used in our experiments, tensile stresses are relatively less efficient in opening microcracks (Winkler, 1996). We assume the rock elastic constants under tensile stress remain the same as in a zero-stress state in our calculation, shown as the dashed line in Figure 2b, in other words, the crack opening is neglected. Our results will show that good results can be obtained with this assumption on Berea sandstone.

LABORATORY EXPERIMENT

In this section, we present results from static strain measurement on Berea sandstone under uniaxial loading to verify the validity and reliability of our numerical approach. The dimensions of the Berea

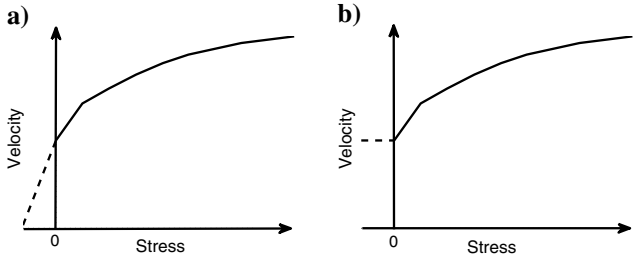

Figure 2. Schematic showing two ways to predict the velocity under tensile stress. Solid curves represent the data measured in a compression (stress > 0) experiment, and dashed lines indicate the extrapolation of data to tensile stress (stress < 0) region. (a) velocity decreases with the decreasing of stress and (b) velocity is constant when stress < 0.

sandstone sample used in this experiment are $101.4 \times 100.6 \times 102.3$ mm^3. The P- and S-wave velocities of the unstressed rock sample were measured in three directions. Figure 3 shows the measured P- and S-waves in three orthogonal directions. We pick the first breaks from the seismograms and calculate the P- and S-wave velocities and find that P- and S-wave anisotropy are only 0.7% and 1.8%, respectively. The measured parameters of the rock are summarized in Table 1.

First, we measure P- and S-wave velocities under varying hydrostatic stress. These data are used to estimate the normal and tangential crack compliances (equations 1 and 2) as functions of hydrostatic pressure, which are required by the method of Mavko et al. (1995). Then, we perform strain-stress measurements of the intact rock under uniaxial loading. This step is to benchmark our measurement setup with the method of Mavko et al. (1995). Finally, we measure the strain-stress behavior of the rock containing a borehole subjected to a gradually increasing uniaxial stress and compare it with our numerical calculations.

Measurement of P- and S-wave velocities under hydrostatic compression

To measure P- and S-wave velocities versus hydrostatic pressure, we cut a 50.8-mm (2-in.)-long and 25.4-mm (1-in.)-diameter cylindrical core from our rock sample that will also be used for the subsequent experiments. We measured P- and S-wave velocities parallel to the core axis. The S-wave velocity measurements were made using two orthogonal polarization directions, as shown in Figure 4. The velocity and hydrostatic pressure have the following empirical relation (Birch, 1961):

$$V = a \log(p) + b, \tag{7}$$

where V represents compressional and shear velocities and p is the hydrostatic pressure, and a and b are coefficients related to the porosity and mineralogy of the rock. We find that equation 7 cannot fit the hydrostatic data very well for pressure <1 MPa, so we modify equation 7 to equation 8 as

$$V = \begin{cases} a_1 p + b_1, & p \le 1 \text{ MPa} \\ a_2 \log(p) + b_2, & p > 1 \text{ MPa} \end{cases}, \tag{8}$$

where a_1, b_1, a_2, and b_2 are constants to be determined through the least-squares method by adding the constraint that the two fitting functions are equal at $p = 1$ MPa. The fits to the P- and S-wave velocities (average of S_1 and S_2) are shown as the blue and red curves, respectively, in Figure 4. Given equation 8, we can now analytically calculate the P- and S-wave velocities at any given hydrostatic pressure.

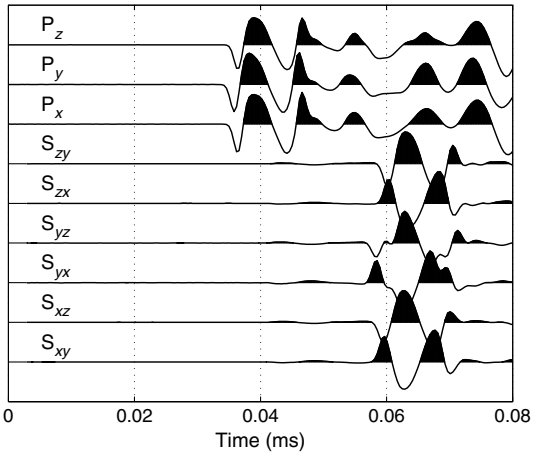

Figure 3. Seismograms recorded for measuring the compressional and shear velocities of the Berea sandstone sample. Acoustic measurements were conducted in three orthogonal directions. $P_i (i = x, y, z)$ indicates the measurement of the P-wave along the i-direction, and $S_{ij} (i, j = x, y, z)$ indicates the measurement of the S-wave along the i-direction with polarization in the j-direction.

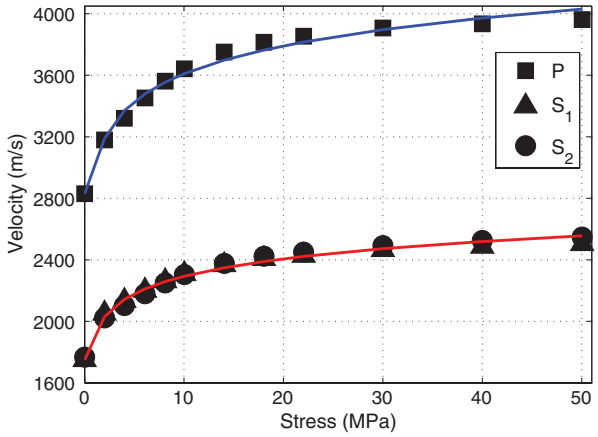

Figure 4. Measurements of P- (squares) and S-wave (triangles and circles) velocities of the Berea sandstone core sample under hydrostatic compression. All measurements were conducted along the core axis direction. Shear wave velocities S_1 and S_2 were measured along the same propagation direction but with orthogonal polarization directions. Blue and red curves are the fitting curves (equation 8) to the P- and S-wave velocities (average of S_1 and S_2), respectively. The root-mean-square misfits are, respectively, 38 and 18 m/s for the fits to the P- and S-wave velocities.

Table 1. Summary of parameters of the Berea sandstone sample in an unstressed state.

Dimensions (mm)	V_P	V_S	Density	Poission's ratio	Porosity	Permeability
$101.4 \times 100.6 \times 102.3$	2.83 km/s	1.75 km/s	2198 kg/m^3	0.19	17.7%	284 mD

Strain measurement of intact rock under uniaxial stress loading

In the intact rock experiment, four 2C strain gauges were mounted at different positions on the rock sample for measuring the normal strains in the directions parallel and normal to the direction of loading stress, as shown in Figure 5 (a photo of our experiment setup). We use standard amplified Wheatstone bridge circuits with an analog-to-digital converter to collect signals from all strain gauges simultaneously. Before performing the experiment, the rock was stress-cycled several times to minimize hysteresis. During the experiment, the uniaxial loading stress was gradually raised from 0 to 10.56 MPa in steps of 0.96 MPa. We limited the maximum loading stress to 10.56 MPa to prevent permanent deformation in the rock. The strains measured under uniaxial loading by the four strain gauges were almost the same. This suggests that the loading stress was evenly distributed on the rock surface.

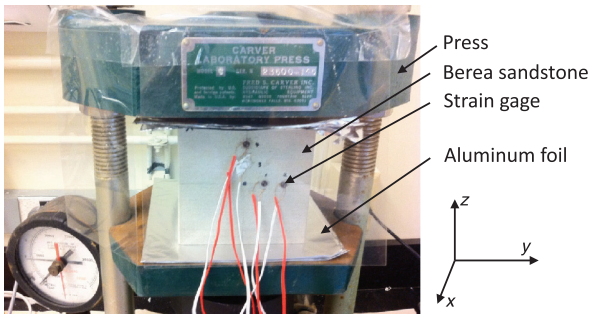

Figure 5. Photo of experiment setup. The Berea sandstone sample has dimensions of $101.4(x) \times 100.6(y) \times 102.3(z)$ mm^3. The size of the strain gauge is about 2 mm. The aluminum foil between the press and the rock is used to make the loading pressure distribution more uniform on the rock surface.

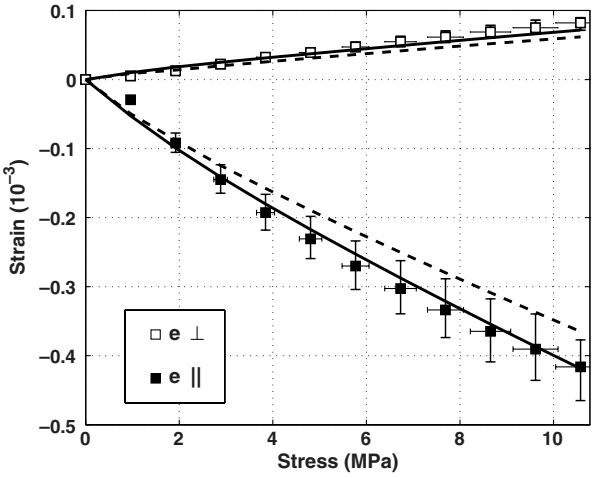

Figure 6. Average normal strains of the intact rock sample under uniaxial loading. Solid and open squares are the measured strain in the directions parallel and normal to the loading stress, respectively. Error bars represent estimates of errors from uncertainty in the measurement of loading stress (~5%) and the error of the gauge factor (~1%). Solid curves and dashed curves are the predicted values obtained from the anisotropic model and isotropic model, respectively.

Figure 6 shows the comparison between the strains (black solid curves) calculated using the method of Mavko et al. (1995) and the measured strains (solid and empty squares). In the direction parallel to the loading axis, the black solid curve (calculated values) matches the solid squares (measured data) very well. In the direction normal to the loading axis, the measured data (empty squares) seem larger

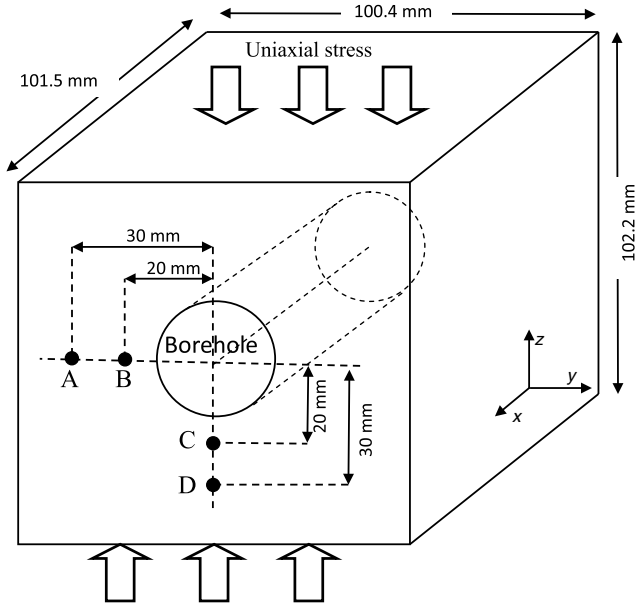

Figure 7. Schematic showing uniaxial stress loading on a rock sample with a borehole. The borehole axis, which is along the x-axis, is normal to the loading stress direction. Strain measurements are conducted at locations A, B, C, and D. B and C are 20 mm away from the borehole center; A and D are 30 mm away from the borehole center. The borehole radius is 14.2 mm.

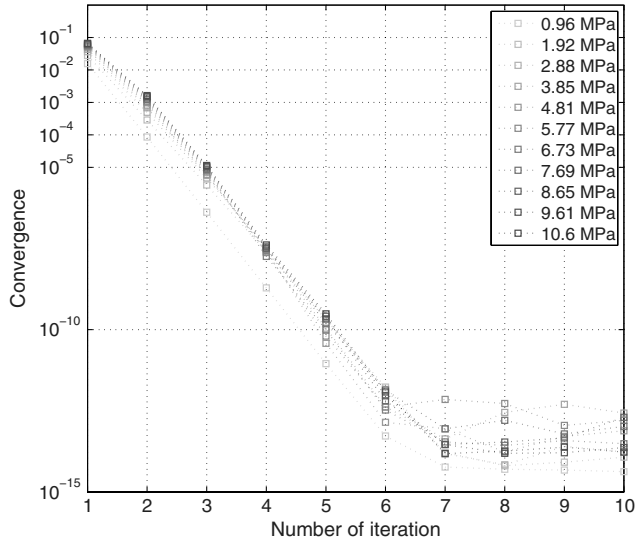

Figure 8. Convergence of the iteration scheme under different loading stress strength. Convergence, which is defined by equation 4, describes the percentage change of the model stiffness after each iteration.

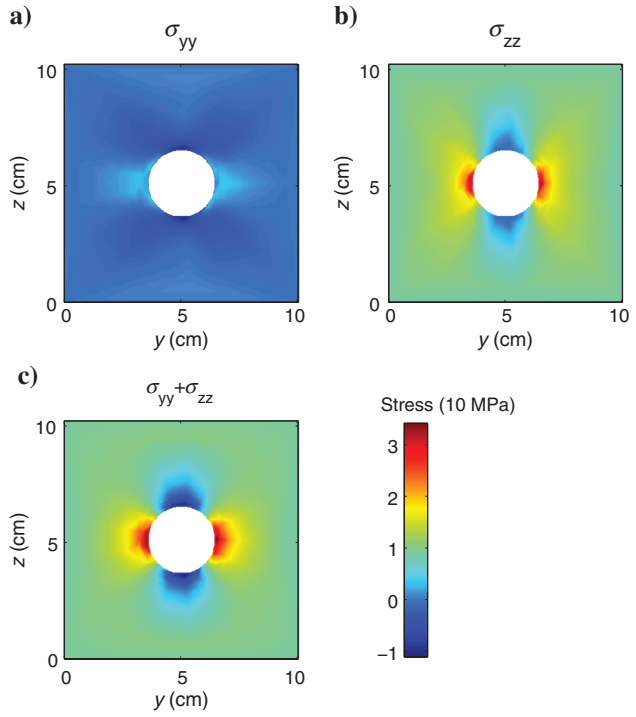

Figure 9. (a), (b) Distribution of σ_{yy} and σ_{zz}, which are the normal stresses in the y- and z-directions, under 10.56 MPa uniaxial stress loading in the z-direction (see Figure 7). (c) Sum of σ_{yy} and σ_{zz}.

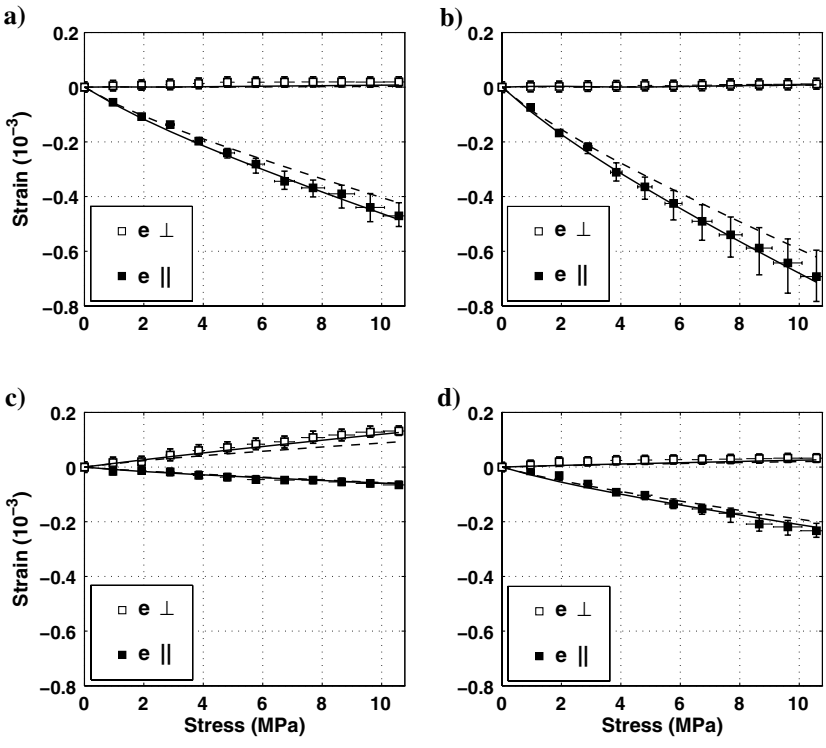

Figure 10. Comparison of laboratory measured strains and numerical results at locations A, B, C, and D, which are shown in Figure 7. Solid and open squares are the measured strain in the directions parallel and normal to the loading stress, respectively. Error bars represent estimates of errors from uncertainty in the measurement of loading stress (~5%) and the error of the gauge factor (~1%). Solid curves and dashed curves are the predicted values obtained from the anisotropic model and isotropic model, respectively.

than the calculated values, especially at higher loading stress ranges. This could be caused by neglecting the effects of the opening of new cracks aligned parallel with the loading axis (Sayers et al., 1990; Mavko et al., 1995). The dashed curves, which are shown for comparison, are the strain values calculated under the assumption that rock properties remain isotropic during the experiment, but V_P and V_S are given by equation 8 in a different stress state, which corresponds to hydrostatic compression and will be referred to as the "isotropic model" hereafter. The absolute values of these dashed curves are always smaller than those of the solid curves. For the isotropic model, the normal stress causes the closure of all cracks independent of orientation, whereas the anisotropic model assumes smaller closure of cracks oriented in directions not perpendicular to the loading direction. Therefore, hydrostatic compression leads to a stiffer rock compared to the rock under uniaxial stress compression.

Strain measurement of the rock with a borehole under uniaxial loading

A borehole with 14.2 mm radius was drilled through the rock along the x-axis at the center of the y-z-plane, as shown in Figure 7. Uniaxial stress, which is applied along the z-axis, is perpendicular to the borehole axis. The stress is also raised in steps of 0.96 MPa up to 10.56 MPa. Strain measurements were made in two orthogonal directions at four locations represented by A, B, C, and D, as shown in Figure 7. We applied our work flow illustrated in Figure 1 and used a FEM software to numerically calculate the stress-induced anisotropy around the borehole subjected to a uniaxial stress.

Figure 8 shows the convergence (equation 4) of the iterations at eleven loading stresses. We found that the convergence is very fast and the change of model stiffness is less than 1% after the first two iterations. We will show the results obtained after the fifth iteration. Figure 9 shows the simulated principal normal stresses σ_{yy} and σ_{zz} on the borehole model surface under 10.56 MPa stress loading in the z direction. Let $\theta = 0^\circ$ define the direction of the applied stress. As seen in Figure 9c, the circumferential stress is highly compressive at $\theta = \pm 90^\circ$ whereas it is tensile at $\theta = 0^\circ$ and 180°. The stress around the borehole now is strongly spatially dependent. As a result, the initially elastic isotropic rock in the unstressed state becomes anisotropic at each point in space due to the varying local stress field.

In Figure 10, the strains measured at four different positions A, B, C, and D are compared to the numerical simulations, similar to Figure 6. We find a good match between the measurements and numerical simulations. Strains measured at B and C, roughly 6 mm away from the borehole edge, are strongly affected by the stress alteration around the borehole. The strain $e_{\|}$ at B in absolute value is much larger than those at A, C, and D, and it reaches a minimum value at C. This is because stress is highly concentrated at B and released at C, as shown in Figure 9b. The strain $e_{\|}$

at D is smaller than that at A. This is again due to the alteration of stress concentration around the borehole. The strain $e_\perp$ always seems to be underestimated in the numerical calculations, perhaps due to the neglect of the crack opening, similar to Figure 6. Our numerical results, however, are a very reasonable match with the measurements. This suggests that the neglect of crack opening has a minor effect in our approach.

Winkler (1996) measures the compressional wave velocity versus azimuth around a borehole in Berea sandstone with and without applied uniaxial stress. In his experiment, a block of Berea sandstone ($150 \times 150 \times 130$ mm) with a 28.6-mm-diameter borehole parallel to the short dimension is saturated in a water tank for conducting acoustic measurements. The P-wave velocity at each azimuth is measured along the borehole axis by using directional transducers. Some properties of the rock are shown in Table 2. Figure 11 shows the measured P-wave velocity versus azimuth with no stress loading (open circles) and with 10 MPa stress loading (solid circles). The P-wave velocity variation with azimuth is very small before applying the stress, and its average value is about 2.54 km/s in the no-stress state. In the experiment of Winkler (1996), the center frequency of the received acoustic signals is about 250 kHz, and the corresponding wave length is 10.2 mm, which is equal to $0.36D$ (D: borehole diameter). We define $\tilde{\lambda} = 0.36D$ as the characteristic wavelength for measuring the P-wave velocity. The size of the rock sample and borehole in our experiment is different from that in the experiment of Winkler (1996); therefore, we compare our results through scaling the model by the borehole diameter. We calculate the spatial distribution of the stiffness tensor of our Berea sandstone borehole model with 10 MPa uniaxial stress applied. The velocity of the P-wave propagating along the borehole axis is mainly governed by the elastic constant C_{1111}, which is shown in Figure 12. From Figure 12, we can see that near the wellbore, the rock becomes stiffer around the regions at $\theta = \pm 90^\circ$, whereas it is relatively softer at $\theta = 0^\circ$ and 180°. Assuming that the P-wave velocity along the x-axis direction is mainly governed by C_{1111}, then the P-wave velocity along the borehole axis direction is given as

$$V_P = \sqrt{\frac{C_{1111}}{\rho}}, \tag{9}$$

where ρ is the density, which is assumed to be independent on the applied stress (Coyner, 1984).

The stress-induced heterogeneities around a borehole could cause dispersion in sonic wave propagation (Sinha and Kostek, 1996; Tang and Cheng, 2004). For a wave with wavelength $\tilde{\lambda} = 0.36D$, the penetration depth of the waves propagating along the borehole wall could be up to $1 \sim 2\tilde{\lambda}$. Here, we first calculate the P-wave velocity by using equation 9 and then average the velocity at each azimuth to obtain the velocity variation with azimuth. The velocity averaging method is shown in Figure 12. In Figure 12, the black circle represents a circular area centered at the wellbore at $\theta = 0^\circ$ with radius r, which represents the penetration depth of the waves, and the velocity at $\theta = 0^\circ$ is taken as the average of the velocity inside the black circle. By moving this black circle from $\theta = 0^\circ$ to 360°, a scan of the velocity versus azimuth can be obtained. By

Table 2. Properties of the rock sample used by Winkler (1996).

V_P (no stress)	Porosity	Permeability
2.54 km/s	22%	510 mD

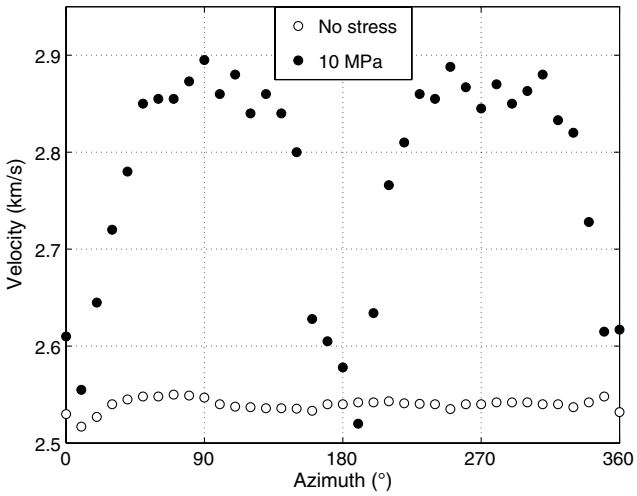

Figure 11. Compressional wave velocity versus azimuth data measured on a Berea sandstone sample with no stress loading (open circles) and with 10 MPa uniaxial stress (solid circles) applied perpendicular to the borehole axis. The values 0° and 180° are along the loading stress direction, and 90° and 270° are normal to the stress direction. Data are taken from Winkler (1996).

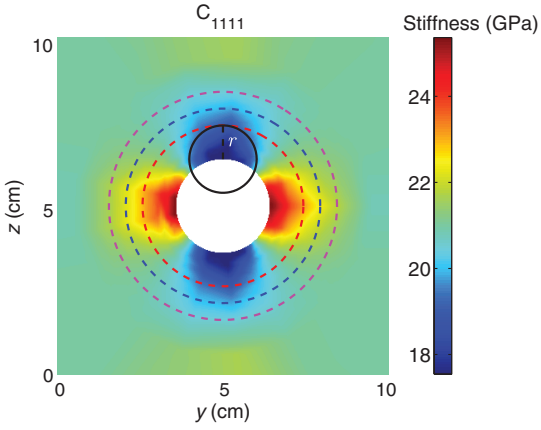

Figure 12. Plot of the elastic constant C_{1111} in the y-z profile under 10 MPa uniaxial stress loading in the z-direction. Circles show how the P-wave velocity is calculated through averaging over a region. The black circle represents a circular region centered at the wellbore at $\theta = 0^\circ$ with radius r, the average of the P-wave velocity inside the circle, not including the white area, is taken as the P-wave velocity at $\theta = 0^\circ$, and the P-wave velocities versus azimuth are obtained by doing this averaging over θ from 0° to 360°. Red, blue, and magenta dashed circles indicate the averaging regions for $r = \tilde{\lambda}$, $1.5\tilde{\lambda}$, and $2\tilde{\lambda}$, respectively.

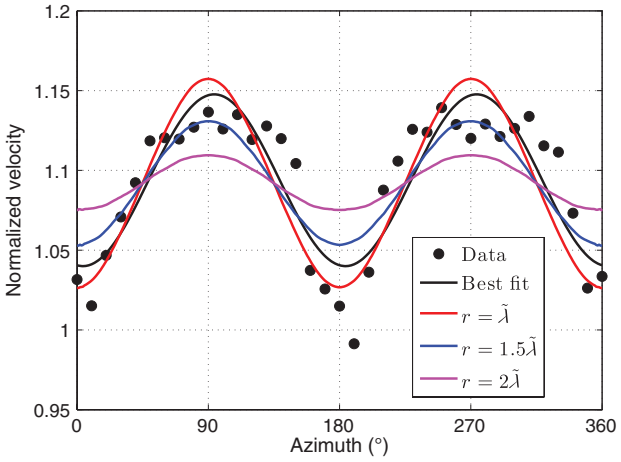

Figure 13. Solid circles are the normalized compressional wave velocity (normalized by the velocity measured at zero stress state) measured by Winkler (1996) under 10 MPa uniaxial stress. The black curve is the best fit to the data by using a cosine function. Red, blue, and magenta curves show the normalized velocities of the Berea sandstone sample used in our experiment by using $r = \tilde{\lambda}$, $1.5\tilde{\lambda}$, and $2\tilde{\lambda}$, respectively, in the averaging.

choosing different values of r, we can obtain the variation of the P-wave velocity around the borehole with different penetration depths. We choose $r = \tilde{\lambda}$, $1.5\tilde{\lambda}$, and $2\tilde{\lambda}$ to do the averaging separately over different areas, which are shown as the red, blue, and magenta circles in Figure 12, respectively. The predicted average velocities normalized by the P-wave velocity with no applied stress are plotted in Figure 13 together with the data measured by Winkler (1996). Winkler (1996) uses a $\cos(2\theta)$ function, shown as the black curve in Figure 13, to fit the data based on the $\cos(2\theta)$ dependence of σ_θ and σ_r on θ in equations 5 and 6. Red, blue, and magenta curves are the velocities obtained from our model by using different averaging radii r. The azimuthal velocity variation decreases away from the wellbore, so a larger averaging radius r gives smaller velocity variation; $r = 1.5\tilde{\lambda}$ could be a reasonable averaging radius. The mismatch between the blue curve and the black best-fit curve is larger at $\theta = 0^\circ$ and 180°. This may be caused by the neglect of the crack opening in our calculation.

CONCLUSIONS

An isotropic rock becomes anisotropic when subjected to an anisotropic applied stress, which causes closure or opening of pores and cracks and induces elastic anisotropy. The presence of a borehole alters the local stress field and leads to inhomogeneous anisotropy distribution around it. In this paper, we present a numerical approach to predict stress-induced anisotropy around a borehole given a stress state by applying a rock physics model. Our method uses hydrostatic data (i.e., V_P and V_S), which are easy to obtain, to calculate the distribution of this stress-induced anisotropy around a borehole. The accuracy of our method is validated through laboratory experiments on a Berea sandstone sample. Our approach can predict the stress-strain relation around a borehole in Berea sandstone under uniaxial stress reasonably well. Our method can be applied to calculate the spatially varying anisotropic elastic constants that are required for the forward modeling of wave propagation in a borehole under a given stress state. Also, this could potentially provide a physical basis for using acoustic cross-dipole logging to estimate the in situ stress state.

ACKNOWLEDGMENTS

We thank D. Burns for helpful discussions. T. Chen was supported by an Earth Resources Laboratory (MIT) Founding Member Postdoctoral Fellowship and a Maersk Fellowship.

REFERENCES

Birch, F., 1961, The velocity of compressional waves in rocks to 10 kilobars, Part 2: Journal of Geophysical Research, **66**, 2199–2224, doi: 10.1029/JZ066i007p02199.

Brace, W., and D. Kohlstedt, 1980, Limits of lithospheric stress imposed by laboratory experiments: Journal of Geophysical Research, **85**, 6248–6252, doi: 10.1029/JB085iB11p06248.

Brown, S., and A. Cheng, 2007, Velocity anisotropy and heterogeneity around a borehole: 77th Annual International Meeting, SEG, Expanded Abstracts, 318–322.

Coyner, K. B., 1984, Effects of stress, pore pressure, and pore fluids on bulk strain, velocity, and permeability in rocks: Ph.D. thesis, Massachusetts Institute of Technology.

Jaeger, J. C., N. G. W. Cook, and R. W. Zimmerman, 2007, Fundamentals of rock mechanics: Blackwell Publishing.

Johnson, P. A., and P. N. J. Rasolofosaon, 1996, Nonlinear elasticity and stress-induced anisotropy in rock: Journal of Geophysical Research, **101**, 3113–3124, doi: 10.1029/95JB02880.

Mao, N. H., 1987, Shear wave transducer for stress measurements in boreholes: U.S. Patent 4,641,520.

Mavko, G., T. Mukerji, and N. Godfrey, 1995, Predicting stress-induced velocity anisotropy in rocks: Geophysics, **60**, 1081–1087, doi: 10.1190/1.1443836.

Oda, M., 1986, An equivalent continuum model for coupled stress and fluid flow analysis in jointed rock masses: Water Resources Research, **22**, 1845–1856, doi: 10.1029/WR022i013p01845.

Oda, M., T. Yamabe, and K. Kamemura, 1986, A crack tensor and its relation to wave velocity anisotropy in jointed rock masses: International Journal of Rock Mechanics and Mining Sciences & Geomechanics Abstracts, **23**, 387–397, doi: 10.1016/0148-9062(86)92304-1.

Sayers, C. M., 1999, Stress-dependent seismic anisotropy of shales: Geophysics, **64**, 93–98, doi: 10.1190/1.1444535.

Sayers, C. M., 2002, Stress-dependent elastic anisotropy of sandstones: Geophysical Prospecting, **50**, 85–95, doi: 10.1046/j.1365-2478.2002.00289.x.

Sayers, C. M., J. Van Munster, and M. King, 1990, Stress-induced ultrasonic anisotropy in Berea sandstone: International Journal of Rock Mechanics and Mining Sciences & Geomechanics Abstracts, **27**, 429–436, doi: 10.1016/0148-9062(90)92715-Q.

Sinha, B. K., and S. Kostek, 1995, Identification of stress induced anisotropy in formations: U.S. Patent 5,398,215.

Sinha, B. K., and S. Kostek, 1996, Stress-induced azimuthal anisotropy in borehole flexural waves: Geophysics, **61**, 1899–1907, doi: 10.1190/1.1444105.

Tang, X. M., and C. Cheng, 2004, Quantitative borehole acoustic methods: Elsevier.

Tang, X. M., N. Y. Cheng, and A. Cheng, 1999, Identifying and estimating formation stress from borehole monopole and cross-dipole acoustic measurement: Presented at SPWLA 40th Annual Logging Symposium, 1099QQ.

Wang, Z., 2002, Seismic anisotropy in sedimentary rocks, Part 2: Laboratory data: Geophysics, **67**, 1423–1440, doi: 10.1190/1.1512743.

Winkler, K. W., 1996, Azimuthal velocity variations caused by borehole stress concentrations: Journal of Geophysical Research, **101**, 8615–8621, doi: 10.1029/96JB00093.

Winkler, K. W., B. K. Sinha, and T. J. Plona, 1998, Effects of borehole stress concentrations on dipole anisotropy measurements: Geophysics, **63**, 11–17, doi: 10.1190/1.1444303.

Zoback, M. D., D. Moos, L. Mastin, and R. N. Anderson, 1985, Well bore breakouts and in situ stress: Journal of Geophysical Research, **90**, 5523–5530, doi: 10.1029/JB090iB07p05523.